Three-dimensional instabilities of liquid-lined elastic tubes: A thin-film fluid-structure interaction model

Joseph P. White[a] and Matthias Heil[b]
Department of Mathematics, University of Manchester, Oxford Road, Manchester M13 9PL, United Kingdom

(Received 3 October 2003; accepted 26 February 2004; published online 1 March 2005)

We develop a theoretical model of surface-tension-driven, three-dimensional instabilities of liquid-lined elastic tubes—a model for pulmonary airway closure. The model is based on large-displacement shell theory, coupled to the equations of lubrication theory, modified to ensure the exact representation of the system's equilibrium configurations. The liquid film that lines the initially uniform, axisymmetric tube can become unstable to a surface-tension-driven instability. We show that, if the surface tension of the liquid lining is sufficiently large (relative to the tube's bending stiffness), the axisymmetric redistribution of fluid by this instability can increase the wall compression to such an extent that the system becomes unstable to a secondary, nonaxisymmetric instability which causes the tube wall to buckle. We establish the conditions for the occurrence of the nonaxisymmetric instability by a linear stability analysis and use finite element simulations to explore the system's subsequent evolution in the large-displacement regime. The simulations show that nonaxisymmetric instabilities allow the formation of occluding liquid bridges in situations in which the volume of fluid is insufficient to occlude the tube in its axisymmetric state. Finally, we discuss the implications of our results for the physiological problem of pulmonary airway closure. © *2005 American Institute of Physics*. [DOI: 10.1063/1.1862631]

I. INTRODUCTION

The pulmonary airways are coated with a thin liquid film that serves many useful functions, such as trapping inhaled particles and protecting the underlying cells from drying.[1] The liquid lining can become unstable to the surface-tension-driven Rayleigh–Plateau instability[2–5] which initiates the redistribution of fluid into axisymmetric lobes. If the film thickness is sufficiently large, the instability can result in the occlusion of the airway with a liquid bridge—a phenomenon known as airway closure.[6]

In the smaller airways, surface tension creates a large pressure jump over the highly curved air-liquid interface which causes a strong compression of the elastic airway walls. The resulting wall deformation reduces the radius of the air-liquid interface and thus facilitates the occurrence of airway closure.[7,8]

In the lungs of a healthy individual, airway closure only occurs in the small airways and at the end of expiration when the airway radii are smallest and hence the liquid lining is thickest. The occluding liquid bridges usually rupture during the early stages of inspiration, a process that gives rise to characteristic "crackling" noises. In many pulmonary diseases, the susceptibility to airway closure is enhanced and occluding liquid bridges may form in larger airways and persist for larger fractions of the breathing cycle. In extreme cases, the airways can remain occluded and this can lead to severe respiratory problems (e.g., the respiratory distress syndrome).

Over the past decade, a number of increasingly sophisticated theoretical models of pulmonary airway closure have been developed in the literature. One of the key objectives has been the determination of the minimum volume of fluid required to form an occluding liquid bridge. Following early work on the Rayleigh–Plateau instability in rigid tubes,[9,3–5] Kamm and Schroter[8] were the first to consider the effects of wall elasticity on pulmonary airway closure. They introduced the concepts of "film collapse" and "compliant collapse" to describe airway closure caused by the classical Rayleigh–Plateau instability and by the surface-tension-driven collapse of the airway wall, respectively. Halpern and Grotberg[7] investigated the interaction between these two mechanisms and studied the occurrence of airway closure via a combined fluid-elastic instability. They showed that wall elasticity significantly reduces the volume of fluid required to occlude an axisymmetric airway. Their study also indicated that the compression induced by the Rayleigh–Plateau instability can cause large axisymmetric airway-wall deformations.

Motivated by the observation that strongly compressed, cylindrical tubes tend to buckle nonaxisymmetrically, Heil[10,11] investigated the static stability of thin-walled, elastic tubes that are occluded by liquid bridges. He showed that the compressive load that a liquid bridge exerts on the airway wall can be strong enough to cause its nonaxisymmetric collapse. Furthermore, he showed that the volume of fluid required to occlude a nonaxisymmetrically buckled airway is much smaller than that required to occlude it in its axisymmetric state.

In the context of the airway closure problem, the mere existence of occluding liquid bridges of small volume does not ensure that such occlusions can be formed via a continu-

[a]Electronic mail: jwhite@maths.man.ac.uk
[b]Author to whom correspondence should be addressed. Electronic mail: M.Heil@maths.man.ac.uk

ous evolution from an initial state in which a uniform liquid film lines the axisymmetric airway wall. The dynamic transition from an axisymmetric (and unoccluded) initial state to a nonaxisymmetrically occluded configuration was first considered by Heil and White[12] who studied the dynamic stability of liquid-lined, elastic rings to nonaxisymmetric perturbations (the analysis also applies to the axially uniform deformation of finite-length tubes). Their study showed that a liquid-lined ring is linearly unstable to nonaxisymmetric perturbations if the compressive load created by the combination of the pleural pressure acting on its outside and the surface tension acting on its inside exceeds a critical value; this is consistent with static analyses of this problem by Hill *et al.*[13] and Rosenzweig and Jensen.[14] Following the onset of nonaxisymmetric instabilities, a strong destabilizing feedback between fluid and solid mechanics was shown to lead to the complete occlusion of the ring's cross section, provided the surface tension was large enough. This demonstrated that, at least in this simplified system, nonaxisymmetric instabilities can lead to the occurrence of airway closure in situations in which there is not enough fluid to occlude the airway in its axisymmetric state.

The present paper extends Heil and White's analysis to three-dimensional instabilities. We show that the increase in wall compression caused by Halpern and Grotberg's primary axisymmetric instability can initiate a secondary nonaxisymmetric instability which causes the local buckling of the airway wall and ultimately results in the formation of a localized occlusion. The mechanism allows the occurrence of airway closure at small fluid volumes and for parameter values for which (i) the axially uniform state is still stable to nonaxisymmetric perturbations and (ii) for which the axisymmetric state remains unoccluded.

II. THE MODEL

We model the airway as an elastic, cylindrical tube of undeformed radius R_0, wall thickness h_w, Young's modulus E, and Poisson ratio ν. The tube is loaded by the external (pleural) pressure p^*_{ext} and it is lined with an incompressible fluid of viscosity μ and constant surface tension σ^*. When the tube is undeformed, the fluid forms a uniform film of thickness $H^*_0=H_0R_0$. Throughout this paper asterisks are used to distinguish dimensional quantities from their nondimensional equivalents.

A. Wall mechanics: Shell theory

We assume that the airway has a small wall thickness, $h_w/R_0 \ll 1$, and use geometrically nonlinear shell theory to describe its deformation in response to the combined load $\mathbf{f}^*$ that the liquid lining and the external pressure exert on it. For this purpose we parametrize the nondimensional vector to the tube's undeformed midplane, $\mathbf{r}_w=\mathbf{r}^*_w/R_0$, by the nondimensional Lagrangian coordinates x^α, measured along the tube's midplane such that $\mathbf{r}_w=[x^1,\sin(x^2),\cos(x^2)]^T$; see Fig. 1. The midplane metric and curvature tensors are given by $a_{\alpha\beta}=\mathbf{a}_\alpha\cdot\mathbf{a}_\beta$ and $b_{\alpha\beta}=\mathbf{n}\cdot\mathbf{a}_{\alpha,\beta}$, respectively, where $\mathbf{a}_\alpha=\mathbf{r}_{w,\alpha}$ and $\mathbf{n}=\mathbf{a}_1\times\mathbf{a}_2$ are the outer normal on the wall. Throughout this paper we use the summation convention and assume

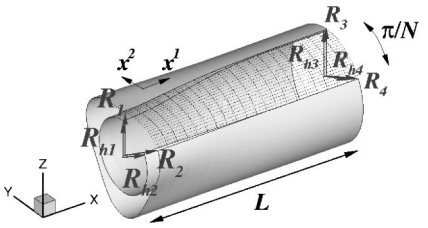

FIG. 1. Sketch of the model problem: A thin-walled elastic tube lined with a liquid film. The tube buckles nonaxisymmetrically in N azimuthal lobes and with an axial wavelength $\Lambda=2L$. Also shown are the Lagrangian coordinates x^α and the control radii used to document the system's evolution.

that, unless specified otherwise, Greek and Latin indices range from 1 to 2 and from 1 to 3, respectively; commas indicate partial differentiation. When the tube deforms, material points are displaced to their new positions $\mathbf{R}_w(x^\alpha)=\mathbf{r}_w(x^\alpha)+\mathbf{v}(x^\alpha)$. We decompose the displacement vector $\mathbf{v}$ into the undeformed basis vectors such that $\mathbf{v}=v^\alpha\mathbf{a}_\alpha+v^3\mathbf{n}$. The tangent and normal vectors to the deformed tube are $\mathbf{A}_\alpha=\mathbf{R}_{w,\alpha}$ and $\mathbf{N}=\mathbf{A}_1\times\mathbf{A}_2/|\mathbf{A}_1\times\mathbf{A}_2|$, and the deformed metric and curvature tensors are $A_{\alpha\beta}=\mathbf{A}_\alpha\cdot\mathbf{A}_\beta$ and $B_{\alpha\beta}=\mathbf{N}\cdot\mathbf{A}_{\alpha,\beta}$, respectively. We denote the determinant of the deformed metric tensor by A.

The buckling of thin cylindrical shells typically involves large displacements and bending deformation but only small in-plane (membrane) deformations. Hence, the components of the bending tensor $\kappa_{\alpha\beta}=-(B_{\alpha\beta}-b_{\alpha\beta})$ can become large whereas the components of the in-plane strain tensor $\gamma_{\alpha\beta}=1/2(A_{\alpha\beta}-a_{\alpha\beta})$ remain small. This implies that the deformed in-plane basis vectors $\mathbf{A}_\alpha$ are approximately unstretched and orthogonal to each other. Hence the strain in the tube wall is small which allows us to use linear constitutive equations (Hooke's law). The principle of virtual displacements which governs the tube's deformation can then be written in the form

$$\int\int\left\{E^{\alpha\beta\gamma\delta}\left[\gamma_{\alpha\beta}\delta\gamma_{\gamma\delta}+\frac{1}{12}\left(\frac{h_w}{R_0}\right)^2\kappa_{\alpha\beta}\delta\kappa_{\gamma\delta}\right]-\frac{1}{12}\frac{1}{(1-\nu^2)}\left(\frac{h_w}{R_0}\right)^2\mathbf{f}\cdot\delta\mathbf{R}_w\sqrt{A}\right\}dx^1dx^2=0 \tag{1}$$

(see, e.g., Ref. 15), where $\mathbf{f}=\mathbf{f}^*/K$ is the load vector, nondimensionalized by the tube's bending stiffness $K=E(h_w/R_0)^3/[12(1-\nu^2)]$ and

$$E^{\alpha\beta\gamma\delta}=\frac{1}{2(1+\nu)}\left(a^{\alpha\gamma}a^{\beta\delta}+a^{\alpha\delta}a^{\beta\gamma}+\frac{2\nu}{1-\nu}a^{\alpha\beta}a^{\gamma\delta}\right) \tag{2}$$

is the plane-stress stiffness tensor. Carrying out the variations with respect to the displacements v^i and their derivatives with respect to the Lagrangian coordinates x^α, transforms (1) into a variational equation of the form

$$\int\int(\phi_i\delta v^i+\phi_{i\alpha}\delta v^i_{,\alpha}+\phi_{i\alpha\beta}\delta v^i_{,\alpha\beta})dx^1dx^2=0, \tag{3}$$

where the functions ϕ depend on the displacements v^i, their first and second derivatives with respect to the Lagrangian coordinates x^α, and on the load vector $\mathbf{f}$ which includes con-

tributions that need to be determined from the fluid mechanics; see (13) below.

If the rotation of material lines in the tube wall is small, the strain and bending tensors can be approximated by Sanders' moderate rotation approximations,[16]

$$\gamma_{11} = (v^1_{,2} - v^2_{,1})^2/8 + v^1_{,1} + (v^3_{,1})^2/2, \tag{4}$$

$$\gamma_{22} = (v^1_{,2} - v^2_{,1})^2/8 + (v^3_{,2} - v^2)^2/2 + v^2_{,2} + v^3, \tag{5}$$

$$\gamma_{12} = \gamma_{21} = (v^1_{,2} + v^2_{,1} + (v^3_{,2} - v^2)v^3_{,1})/2, \tag{6}$$

and

$$\kappa_{11} = -v^3_{,11}, \quad \kappa_{22} = v^2_{,2} - v^3_{,22}, \tag{7}$$

$$\kappa_{12} = \kappa_{21} = -v^3_{,12} - v^1_{,2}/4 + 3v^2_{,1}/4. \tag{8}$$

We will use these approximations in the stability analyses in Secs. III A and IV A.

B. Fluid mechanics: Lubrication theory

To describe the surface-tension-driven flow in the liquid film that lines the deforming tube, we parametrize the fluid domain by introducing a vector $\mathbf{R}_f$ to a point at a distance x^3 from the inner surface of the tube via

$$\mathbf{R}_f(x^1,x^2,x^3,t) = \mathbf{R}_w(x^1,x^2,t) + x^3\mathbf{S}_f(x^1,x^2,t). \tag{9}$$

In this parametrization, the air-liquid interface is located at $x^3 = h(x^1,x^2,t)$, where the film thickness h is measured in the direction of the vector $\mathbf{S}_f$, defined as

$$\mathbf{S}_f = \frac{1}{\sqrt{(N_2)^2 + (N_3)^2}}(0, -N_2, -N_3)^T. \tag{10}$$

The volume of fluid "above" a patch bounded by the Lagrangian coordinate increments dx^1 and dx^2 on the inner surface of the tube is then given by $dV = M dx^1 dx^2$ where

$$M(x^1,x^2,t) = \int_0^{h(x^1,x^2,t)} \sqrt{g}\, dx^3, \tag{11}$$

and g is the determinant of the metric tensor $g_{ij} = \mathbf{R}_{f,i} \cdot \mathbf{R}_{f,j}$ associated with the parametrization (9).

If we assume that the film thickness h is (and remains) much smaller than the minimum radii of curvature of the wall and the air-liquid interface, and that the Reynolds number of the surface-tension-driven flow is small, then the evolution of the film thickness can be described by lubrication theory (see, eg., Ref. 17),

$$\frac{\partial M}{\partial \hat{t}} - \frac{\partial}{\partial x^\alpha}\left(\frac{1}{3}h^3 \frac{\partial \kappa_h}{\partial x^\alpha}\right) = 0, \tag{12}$$

where we have used the assumption that coordinate lines remain approximately orthogonal and unstretched—this is consistent with the small-strain assumption already made in the wall mechanics. $\kappa_h = \kappa_h^* R_0$ is the curvature of the air-liquid interface (the sign chosen such that $\kappa_h < 0$ for the initial uniform film) and time has been nondimensionalized on the viscous scale, $\hat{t} = t^*/(\mu R_0/\sigma^*)$. The fluid pressure is constant through the thickness of the film. We use the pressure in the airway lumen as the reference value and set it to zero. Then the (dimensional) fluid pressure is given by $p^* = \kappa_h \sigma^*/R_0$.

The assumptions underlying the derivation of (12) from the three-dimensional (3D) Navier–Stokes equations imply that κ_h could be linearized with respect to the film thickness h and the wall displacements v^i without loss of (asymptotic) accuracy in the limit $h, v^i \to 0$. Furthermore, $\partial M/\partial \hat{t}$ could be replaced by $\partial h/\partial \hat{t}$. However, it was shown in Refs. 9 and 12 that Eq. (12) provides excellent predictions for the evolution of the air-liquid interface even if the film thickness becomes large and/or the tube wall highly curved, provided the exact expressions for κ_h and M are used (see Fig. 16 in Appendix A for an illustration). This is because surface-tension-driven flows evolve towards equilibrium configurations in which the air-liquid interface has uniform curvature. Using the exact expressions for M and κ_h ensures that these equilibrium configurations are represented accurately by (12): $\partial/\partial t = 0$ if and only if $\kappa_h = \text{const}$, subject to the constraint that the volume of fluid is conserved.

C. Fluid structure interaction

Fluid and solid mechanics interact in two ways: (i) The wall displacements change the geometry of the fluid domain. This effect is represented by its parametrization via Eq. (9). Hence, M and κ_h in the evolution equation (12) for the film thickness h also depend on the wall displacements v^i. (ii) The wall is exposed to the fluid pressure p^* and the flow in the liquid film generates a wall shear stress. If we measure the external pressure $p_{ext} = p^*_{ext}/K$ relative to the pressure in the airway lumen then the combined load on the airway wall is given by

$$\mathbf{f} = -p_{ext}\mathbf{N} + \sigma\left(\kappa_h \mathbf{N} - h\frac{\partial \kappa_h}{\partial x^\alpha}\mathbf{A}_\alpha\right), \tag{13}$$

where we have again exploited the fact that the Lagrangian coordinate lines remain approximately orthogonal and unstretched. The parameter

$$\sigma = \frac{\sigma^*}{KR_0} \tag{14}$$

is the nondimensional surface tension and represents the ratio of the typical pressure jump over the curved air-liquid interface to the wall's bending stiffness. Large values of σ indicate strong fluid-structure interaction.

Equation (13) shows that the initial load on the undeformed airway is given by the pressure

$$p_{init} = p_{ext} + \frac{\sigma}{1 - H_0}. \tag{15}$$

Increases in σ and/or H_0 increase the initial wall compression and thus make the wall more susceptible to buckling instabilities. When we consider the effect of variations in σ and H_0, we will usually compensate for this (obvious) destabilizing effect by adjusting the external pressure so that the tube remains subject to the same initial compression p_{init}. This procedure allows a clearer identification of the various additional instability mechanisms that are involved in non-

axisymmetric airway closure. Interestingly, the procedure has a strong resemblance to the clinical procedure of positive-end-expiratory-pressure ventilation in which the destabilizing effect of a pathological increase in the surface tension of the lung's liquid lining is compensated for by an artificial pressurization of the lung.

D. Presentation of the results

The time scale, $T_{visc}=\mu R_0/\sigma^*$, that we used for the nondimensionalization of the fluid equation (12) yields a parameter-free partial differential equation but T_{visc} does not capture the dynamics of the surface-tension-driven thin-film flows. The time scale for such flows is given by $T_{lubri}=3\mu R_0/(\sigma^* H_0^3)$, provided the wall deformation and the changes in the film thickness remain small. We wish to analyze the effect of variations in H_0 and σ^* in problems with strong fluid-structure interaction. Therefore we shall present most of our results on a third time scale, $t=t^*/T$ where $T=\mu/K$ which is independent of these quantities.

To illustrate the temporal evolution of the system, we will frequently show plots of the radii of the eight characteristic points (four on the tube wall and four on the air-liquid interface) identified in Fig. 1. These radii allow a simple characterization of the system's deformation. For instance, nonaxisymmetric buckling of the tube wall in the cross section $x=0$ manifests itself by a decrease in R_1 and an increase in R_2 whereas $R_1 \approx R_2$ indicates that the cross section has remained approximately axisymmetric.

The simulations presented below were performed with a nondimensional wall thickness of $h_w/R_0=1/20$. This value represents a compromise between the values in the pulmonary airways (which tend to be slightly thicker) and the limitations imposed by the use of thin-shell theory. Poisson's ratio was set to $\nu=0.49$ to reflect the near-incompressibility of physiological tissue.

III. THE PRIMARY AXISYMMETRIC INSTABILITY

We will first (re)investigate the axisymmetric instability of liquid-lined elastic tubes (first studied by Halpern and Grotberg[7]) with our formulation. The results from this section form the basis for Sec. IV A in which we analyze the linear stability of the evolving axisymmetric state to nonaxisymmetric perturbations.

A. Linear stability analysis

Initially, the fluid forms a static, uniform film on the axisymmetric tube wall. In this configuration, the relation between the external pressure p_{ext} and the uniform radial wall displacement $v^3=V_0$ is given by

$$p_{ext} = -\frac{12}{(h_w/R_0)^2}\frac{V_0}{1+V_0} - \frac{\sigma}{1+V_0-\tilde{H}_0}, \tag{16}$$

where we have used Sanders' moderate rotation approximations for the strain and bending tensors.

$$\tilde{H}_0 = 1 + V_0 - \sqrt{(1+V_0)^2 + H_0(H_0-2)} \tag{17}$$

is the uniform film thickness on the deformed tube. $\tilde{H}_0$ increases when the tube is compressed. To determine the stability of this uniform state to axisymmetric perturbations, we expand the film thickness h and the wall displacements v^i as

$$h = h^{(0)} = \tilde{H}_0 + \epsilon_A H^{(A)} e^{\omega \hat{t}} \cos(kx^1), \tag{18}$$

$$v^1 = v^{(0)1} = \epsilon_A V^{(A)1} e^{\omega \hat{t}} \sin(kx^1), \tag{19}$$

$$v^2 = 0, \tag{20}$$

$$v^3 = v^{(0)3} = V_0 + \epsilon_A V^{(A)3} e^{\omega \hat{t}} \cos(kx^1), \tag{21}$$

where $\epsilon_A \ll 1$. We insert (18)–(21) into the Euler–Lagrange equations of the variational principle (1), into the fluid equation (12), and into the load terms (13) and expand all equations in powers of ϵ_A. At order $O(\epsilon_A)$ we obtain three linear algebraic equations which can be written in matrix form as $\mathbf{Sy}=\mathbf{0}$ where $\mathbf{y}=(V^{(A)1}, V^{(A)3}, H^{(A)})$ is the vector of the perturbation amplitudes. The temporal growth rate ω of the perturbation with axial wavenumber $k=2\pi/\Lambda$ is determined by $\det(\mathbf{S})=0$. The exact expression for the growth rate ω is too lengthy to quote here but it has the form

$$\omega = \frac{\tilde{H}_0^3 k^2}{3(1+V_0-\tilde{H}_0)}\left(\frac{1}{(1+V_0-\tilde{H}_0)^2} - k^2\right) \times \left\{1 + O\left[\sigma\left(\frac{h_w}{R_0}\right)^2\right]\right\}. \tag{22}$$

This shows that the neutrally stable wavenumber k_{neutr} is the reciprocal of the radius of the axially uniform interface,

$$k_{neutr} = 1/(1+V_0-\tilde{H}_0), \tag{23}$$

and perturbations with $k<k_{neutr}$ have positive growth rates. This is completely analogous to the behavior found in rigid tubes.[17] If we let the wall bending stiffness $K\to\infty$ (by setting $\sigma=0$), Eq. (22) becomes identical to the dispersion relation for perturbations to liquid films that line uniform rigid tubes. In that case the maximum growth rate ω_{max} occurs for perturbations with wavenumber $k_{max}=2\pi/\Lambda_{max}=1/[\sqrt{2}(1-H_0)]$. The plot of the dispersion relation (22) for various values of σ in Fig. 2 shows that wall elasticity ($\sigma>0$) slightly increases the growth rate of the fastest growing instability and slightly decreases its wavenumber.

Qualitatively, these predictions agree with Halpern and Grotberg's results for the case of zero wall damping ($\phi=0$ in their model). A direct comparison is difficult because Halpern and Grotberg's model is based on different wall equations; see Appendix C for a more detailed discussion.

B. Numerical simulation in the nonlinear regime

1. Discretization

To follow the evolution of unstable axisymmetric perturbations into the large-displacement regime, we set $\partial/\partial x^2=0$ and $v^2=0$ and discretized the wall and fluid equations (1) and (12) in the domain $x^1 \in [0,L]$ with finite elements. We ap-

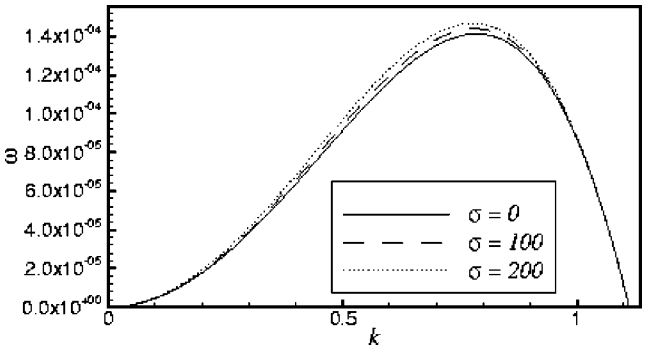

FIG. 2. The dispersion relation for axisymmetric perturbations to axially uniform liquid-lined tubes for different nondimensional surface tensions σ: Growth rate $\omega=\omega^*\mu R_0/\sigma^*$ as a function of the wavenumber k. $p_{init}=0$, $H_0=0.1$.

plied periodic boundary conditions that allow the development of the fastest growing perturbation and set $(v^1=v^3_{,1}=h_{,1}=\kappa_{h,1}=0)$ at $x^1=0$ and $x^1=L$. Generally we set $L=\sqrt{2}\pi(1-H_0)$, half the wavelength of the fastest growing perturbation to the film thickness in a rigid tube because wall elasticity only has a small effect on the most unstable wavelength; see Fig. 2. We will investigate the effect of variations in the domain length L in Sec. IV B. The procedure employed for the discretization of the coupled equations is based on that used in Ref. 12 where full details can be found. Briefly, we represent the axial and radial wall displacements by piecewise cubic Hermite polynomials $\psi_j(x^1)$ and write

$$v^{(0)i}(x^1,\hat{t})=\sum_j V^{ij}(\hat{t})\psi_j(x^1) \text{ for } i=1 \text{ and } 3. \tag{24}$$

We insert these expansions into the variational principle (3) which becomes

$$\left\{\int_0^L(\phi_i\psi_j+\phi_{i1}\psi_{j,1}+\phi_{i11}\psi_{j,11})dx^1\right\}\delta V^{ij}=0. \tag{25}$$

The variations of those V^{ij} that are not determined by the periodicity conditions are arbitrary and the expressions multiplied by the corresponding δV^{ij} must vanish. This provides a system of nonlinear algebraic equations for the unknown V^{ij}. These equations still contain the load terms $\mathbf{f}$, which have to be determined from the solution of the fluid equations.

Equation (12) involves the second derivative of the interface curvature κ_h which itself contains second derivatives of the wall displacement field v^i. Fourth derivatives of the wall displacement field are not available from the Hermite expansion in (24). Therefore, Eq. (12) was solved by a mixed finite element method in which independent Hermite interpolations were used for the film's thickness and its curvature,

$$h(x^1,\hat{t})=\sum_j H^j(\hat{t})\psi_j(x^1), \quad \tilde{\kappa}_h(x^1,\hat{t})=\sum_j K^j(\hat{t})\psi_j(x^1). \tag{26}$$

The finite element expansion $\tilde{\kappa}_h$ for the film curvature was then used in the Galerkin solution of the weak form of (12) which was integrated by parts to yield the equations

$$f_j^{(H)}=\int_0^L\left(\frac{\partial M}{\partial\hat{t}}\psi_j+\frac{h^3}{3}\frac{\partial\tilde{\kappa}_h}{\partial x^1}\frac{\partial\psi_j}{\partial x^1}\right)dx^1=0. \tag{27}$$

After discretizing the time derivative with an adaptive BDF2 scheme,[18] this provides a system of discrete equations for those H^j which are not determined by the periodicity conditions. The equations were augmented by the weak equations for the discrete curvatures K^j,

$$f_j^{(K)}=\int_0^L\left(\sum_l K^l\psi_l-\kappa_h\right)\psi_j dx^1=0, \tag{28}$$

where κ_h is the exact curvature of the air-liquid interface. Newton's method was used to solve the fully coupled system of nonlinear algebraic equations that arise at each time step. The associated linear systems were solved with the frontal solver HSL_MA42 from the HSL2000 library.[19] The simulations were started from an initial state in which $v^1=v^3=0$ and $h=H_0[1+\epsilon_h\cos(\pi x^1/L)]$, where $\epsilon_h=10^{-2}$ was used to initiate the growth of the instability in a controlled manner.

To validate the numerical solution of the wall equations, we considered the deformation of a finite-length tube with clamped ends, subject to a constant external pressure. We compared the predictions for the wall displacement field obtained from the finite-element based discretization of the variational principle (3) against independent solutions obtained from a finite-difference discretization of the corresponding Euler–Lagrange equations. When plotted, the results were graphically indistinguishable. To validate the numerical solution of the lubrication theory equations (12), we compared the initial growth rates of the axisymmetric instability against those predicted by the dispersion relation (22). Furthermore, we repeated Gauglitz and Radke's[9] simulations of the finite-amplitude evolution of the Rayleigh–Plateau instability in rigid tubes (simulated here by setting $\sigma=0$, which corresponds to the case of infinite wall stiffness) and obtained excellent agreement with their results (see Ref. 20). Finally, we performed (qualitative) comparisons with Halpern and Grotberg's simulations;[7] see Appendix C for details. The independence of all results on the time step and the spatial resolution was confirmed.

2. Results

Figures 3 and 4 illustrate the system's evolution for $H_0=0.1$ and $\sigma=100$: Initially, the perturbation to the film thickness grows exponentially and fluid drains into a main lobe which is centered at $x=0$; see Fig. 3(a). As the volume of the main lobe increases, the film thins in the right half of the domain and in Fig. 3(b), the development of a secondary (satellite) lobe can be observed. The main and satellite lobes are connected by a rapidly thinning "neck" region. The flow resistance in this region increases with h^{-3}, hence the flux into the main lobe decreases rapidly even though the pressure drop between the two lobes continues to increase (see the right column in Fig. 3 which shows the normal component, $p_{ext}-\sigma\kappa_h$, of the load on the wall; since p_{ext} remains constant, the graph gives an indication of the variations in the interface curvature and the fluid pressure). Figure 3(c) shows the shape of the interface at large times, together with

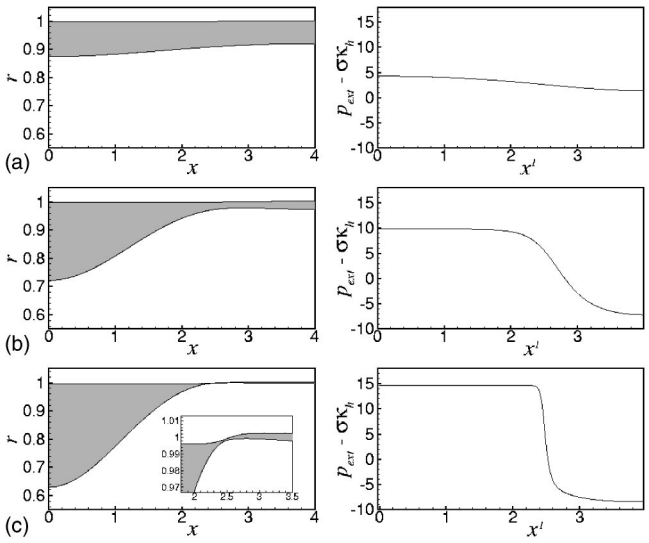

FIG. 3. The axisymmetric fluid domain (left column) and the normal component of the load on the wall (right column) at different times. (a) $t=2.20\times10^2$, (b) $t=5.0\times10^2$, and (c) $t=4.95\times10^4$. The inset in (c) shows a closeup of the thin "neck" region that connects the main and satellite lobe. $H_0=0.1$, $\sigma=100$, $p_{init}=2.9$, $L=\sqrt{2}\pi(1-H_0)$. Time scale $t=t^*/(\mu/K)$.

a closeup of the thin neck region. The corresponding plot of the wall load indicates that the fluid in the main lobe exerts a strong compression on the tube wall. The air-liquid interface curvature in the satellite lobe is approximately uniform but less negative than in the initial, axially uniform configuration. Consequently, the tube wall is inflated in this region.

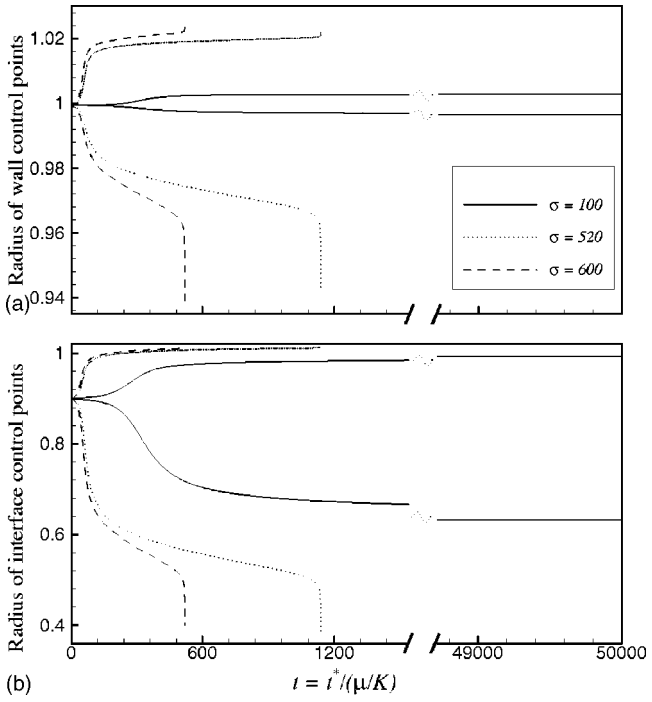

FIG. 4. (a) The wall radii R_1 (lower lines) and R_3 (upper lines), and (b) the corresponding radii of the air-liquid interface during the axisymmetric Rayleigh instability for different values of the surface tension σ. When $\sigma=100$, an axisymmetric lobe forms which does not occlude the airway. As the surface tension is increased, the airway can undergo compliant collapse leading to airway closure. $H_0=0.1$, $L=\sqrt{2}\pi(1-H_0)$, $p_{init}=2.9$.

The system is not in equilibrium but the time scale for the further redistribution of fluid is very large. This is illustrated by the solid lines in Fig. 4, which show the evolution of the radii R_1, R_3, R_{h1}, and R_{h3}: as the perturbation grows, R_{h1} (R_{h3}) decreases (increases) as fluid drains into the main lobe. The compression of the tube near $x=0$ reduces R_1 while the reduced interface curvature near $x=L$ inflates the tube and thus increases R_3. In its axisymmetric state, the tube wall is very stiff and despite the strong compression near $x=0$, the wall only undergoes very small radial deflections. Therefore, the redistribution of the fluid is very similar to that observed in rigid tubes for which it was shown by Gauglitz and Radke,[9] that an initial film thickness of at least $H_0\approx0.12$ is required to allow the formation of an occluding liquid bridge via a continuous evolution from the initial uniform liquid film. For smaller values of H_0, fluid continues to drain from the satellite lobe into the main lobe whose air-liquid interface ultimately approaches the shape of an unduloid—a surface of constant mean curvature.[2] In practice, van der Waals forces would cause the film to rupture in the neck region when the film thickness falls below a critical value. This would create two disconnected lobes which are separated by a dry patch. However, this effect is not included in our model.

The broken lines in Fig. 4 show the evolution of the four control radii when the nondimensional surface tension is increased. As discussed in Sec. II D, we adjusted the external pressure so that the initial compression p_{init} is the same for all cases. The additional wall compression generated by the axisymmetric redistribution of fluid is given by the product of the surface tension σ and the change in interface curvature relative to its value in the axially uniform state. Hence, for a given shape of the air-liquid interface, an increase in σ increases the additional wall compression. In an elastic tube, this reduces the radii of the wall and the air-liquid interface and increases the wall compression even further. Figure 4 shows that, for sufficiently large values of the nondimensional surface tension σ, this destabilizing feedback can initiate an irreversible and extremely rapid collapse of the air-liquid interface. The occurrence of airway closure via this mechanism was first identified and studied by Halpern and Grotberg.[7]

IV. THE SECONDARY NONAXISYMMETRIC INSTABILITY

The preceding section showed that the redistribution of fluid by the primary axisymmetric instability creates a strong compression of the airway wall in the region of the main lobe. We will now investigate whether this compressive load can become large enough to initiate a secondary nonaxisymmetric instability that causes the buckling of the airway wall. We are particularly interested in parameter regimes in which airway closure either by Halpern and Grotberg's axisymmetric mechanism or by Heil and White's nonaxisymmetric, but axially uniform mechanism is impossible.

A. Linear stability analysis

1. Formulation and numerical solution

We decompose the wall displacement field into its axisymmetric part and a small nonaxisymmetric perturbation by writing $v^i = v^{(0)i}(x^1;t) + \epsilon v^{(1)i}(x^1,x^2,t)$, where $\epsilon \ll 1$. As shown in Sec. III B, the axisymmetric state $v^{(0)i}$ evolves in time but it evolves slowly, except during the very early stages of the system's evolution or when (and if) it undergoes the final, very rapid collapse. We wish to analyze the system's stability to nonaxisymmetric perturbations in the intermediate regime. Therefore we determine the growth rate of the nonaxisymmetric perturbations, $v^{(1)i}$, by a "frozen-coefficient" analysis and write the nonaxisymmetric perturbations as

$$
\begin{aligned}
v^{(1)1}(x^1,x^2,t) &= \mathcal{V}^{(1)1}(x^1)\cos(Nx^2)e^{\xi t},\\
v^{(1)2}(x^1,x^2,t) &= \mathcal{V}^{(1)2}(x^1)\sin(Nx^2)e^{\xi t},\\
v^{(1)3}(x^1,x^2,t) &= \mathcal{V}^{(1)3}(x^1)\cos(Nx^2)e^{\xi t},
\end{aligned}
\tag{29}
$$

where N is the (integer) azimuthal wavenumber of the mode with axial mode shape $\mathcal{V}^{(1)i}(x^1)$.

We apply equivalent perturbation to the film thickness and the air-liquid interface curvature by writing

$$
\begin{aligned}
h^{(1)}(x^1,x^2,t) &= h^{(0)}(x^1;t) + \epsilon\mathcal{H}^{(1)}(x^1)\cos(Nx^2)e^{\xi t},\\
\kappa_h^{(1)}(x^1,x^2,t) &= \kappa_h^{(0)}(x^1;t) + \epsilon\mathcal{K}^{(1)}(x^1)\cos(Nx^2)e^{\xi t},
\end{aligned}
\tag{30}
$$

and determine the instantaneous growth rates $\lambda = \mathrm{Re}(\xi)$ of these modes for a given (frozen) axisymmetric solution $v^{(0)i}(x^1;t)$. Consistency of the variations δv^i in (3) with (29) requires that

$$
\begin{aligned}
\delta v^1 &= \cos(Nx^2)\,\delta\mathcal{V}^{(1)1}(x^1),\\
\delta v^2 &= \sin(Nx^2)\,\delta\mathcal{V}^{(1)2}(x^1),\\
\delta v^3 &= \cos(Nx^2)\,\delta\mathcal{V}^{(1)3}(x^1),
\end{aligned}
\tag{31}
$$

where $\delta\mathcal{V}^{(1)i}$ are arbitrary. With these expansions, Eqs. (12) and (13) only have a trivial (and consistent) x^2 dependence, and the integration over x^2 in (3) can be carried out analytically. We expand all terms in (3), (12), and (13) in powers of ϵ and, upon collecting the linear terms, we obtain a spatially one-dimensional, linear eigenvalue problem for the mode shapes $\mathcal{V}^{(1)i}(x^1)$, $\mathcal{H}^{(1)}(x^1)$, and $\mathcal{K}^{(1)}(x^1)$. The coefficients in this eigenvalue problem depend on the primary axisymmetric solution which is only available numerically from the procedure discussed in Sec. III B. Therefore we expand the mode shapes $\mathcal{V}^{(1)i}(x^1)$, $\mathcal{H}^{(1)}(x^1)$, and $\mathcal{K}^{(1)}(x^1)$ in the same finite element bases (24) and (26) that we used for the discretization of the axisymmetric problem. This transforms the continuous problem into a discrete generalized eigenvalue problem of the form

$$
(\mathbf{A} - \xi\mathbf{B})\mathbf{x} = \mathbf{0}, \tag{32}
$$

where $\mathbf{A}$, $\mathbf{B}$ are sparse matrices, and $\mathbf{x}$ is the vector containing the degrees of freedom of the finite element expansion for the mode shapes. The matrices have no special symmetries and we used the generalized non-Hermitian eigenvalue routine nag_nsym_gen_eig_all from the NAG library to compute the eigenvalues and eigenvectors.

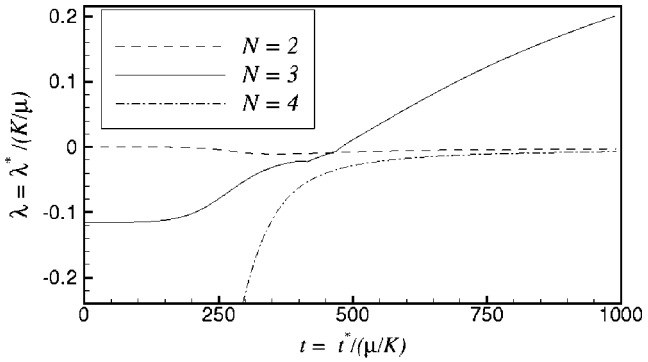

FIG. 5. The maximum growth rate λ against time t for the nonaxisymmetric modes $N=2,3,4$. The system becomes unstable to nonaxisymmetric perturbations in the $N=3$ mode at $t\approx 480$. $\sigma=100$, $H_0=0.1$, $p_{init}=2.9$, $L=\sqrt{2}\pi(1-H_0)$.

We validated the stability analysis by determining the tube's stability to nonaxisymmetric perturbations when loaded by a constant external pressure (i.e., for $\sigma=0$). The buckling pressures and the associated mode shapes for various azimuthal and axial wavenumbers agreed with the predictions of Ref. 21 to within 1%. Furthermore, we compared the growth rates of nonaxisymmetric, but axially uniform, perturbations to the analytical predictions of Ref. 12. The predictions for the growth rates agreed to within 2%. Finally, we compared the predictions for the onset of nonaxisymmetric instabilities with the numerical solution of the full nonlinear equations; see Sec. IV B.

2. Results

Figure 5 illustrates the stability of the evolving axisymmetric configuration to nonaxisymmetric perturbations. The figure was generated by the following procedure: starting from the same initial conditions that we used for the simulation shown in Fig. 3, we (re)computed the system's axisymmetric evolution. At every time step, we evaluated the coefficients of the eigenvalue problem (32) and determined the growth rates $\lambda = \mathrm{Re}(\xi)$ for perturbations with various azimuthal wavenumbers N. Figure 5(a) shows the largest instantaneous growth rates $\lambda(N)$ for nonaxisymmetric perturbations with azimuthal wavenumbers $N=2,3,4$, as a function of time. Initially, all growth rates are negative and the system is stable to nonaxisymmetric perturbations. As the axisymmetric lobe develops, the tube's compression increases (see Fig. 3) and at $t\approx 480$ the tube becomes unstable to nonaxisymmetric buckling in the $N=3$ mode. The axisymmetric lobe continues to grow, increasing the compressive load on the central part of the tube even further. This increases the growth rate of the unstable $N=3$ mode while the growth rates of all other modes remain negative.

Figure 6 shows a plot of the maximum growth rate λ against time for different values of σ. We only plot the value of the growth rate when it is positive and all curves are for the $N=3$ mode, as perturbations with other azimuthal wave-

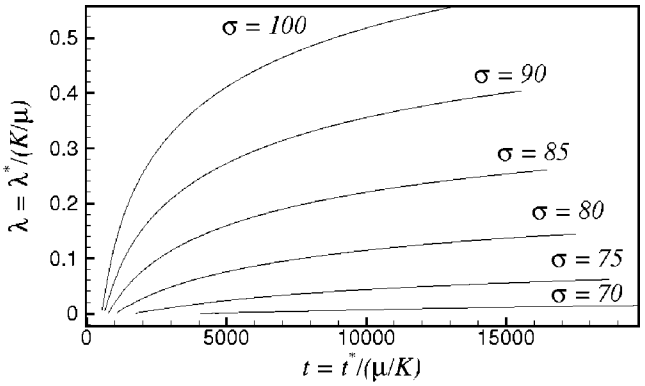

FIG. 6. The positive growth rates λ of perturbations with azimuthal wavenumber $N=3$ against time t for different values of the surface tension σ. $p_{init}=2.9$, $H_0=0.1$, $L=\sqrt{2}\pi(1-H_0)$.

numbers decay. As σ decreases, the onset of the nonaxisymmetric instability is delayed and its growth rate is reduced. This is documented in more detail in Fig. 7 which shows how the time t_{instab}, at which the system first becomes unstable to nonaxisymmetric perturbations, varies with σ. The figure suggests that the system will remain stable to nonaxisymmetric perturbations if σ is less than some critical value σ_{min}. This quantity is of interest in the context of the airway closure problem because, if the values of p_{init} and H_0 are such that the airway cannot become occluded in its axisymmetric state then airway closure is impossible if $\sigma<\sigma_{min}$. (For the values chosen here, the solid curves in Fig. 4 show that this is indeed the case and Fig. 7 suggests that $\sigma_{min}\leq 63$).

As discussed in Sec. III B, the wall compression increases continuously as the fluid redistributes itself towards its final axisymmetric equilibrium state in which its entire volume is contained in a single lobe. For values of σ close to σ_{min}, the main lobe has to be almost fully developed before the wall compression is strong enough to cause buckling. The evolution towards this final state takes place over extremely long time scales and the presence of the increasingly thin neck region that connects the main and satellite lobes requires the use of very fine spatial discretizations to fully resolve the flow. Therefore it is not feasible to compute the value of σ_{min} by continuing the procedure used to obtain the

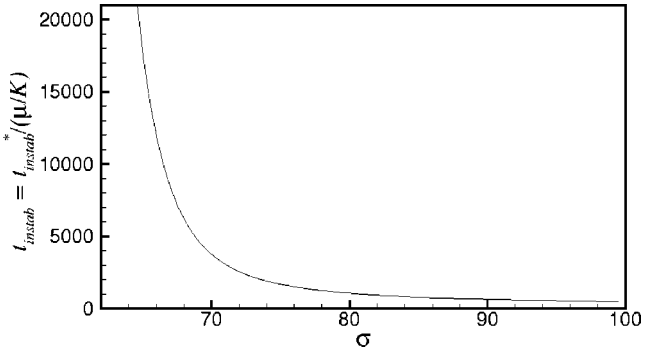

FIG. 7. The time at which the system becomes unstable to nonaxisymmetric perturbations as a function of the surface tension σ. $p_{init}=2.9$, $H_0=0.1$, $L=\sqrt{2}\pi(1-H_0)$.

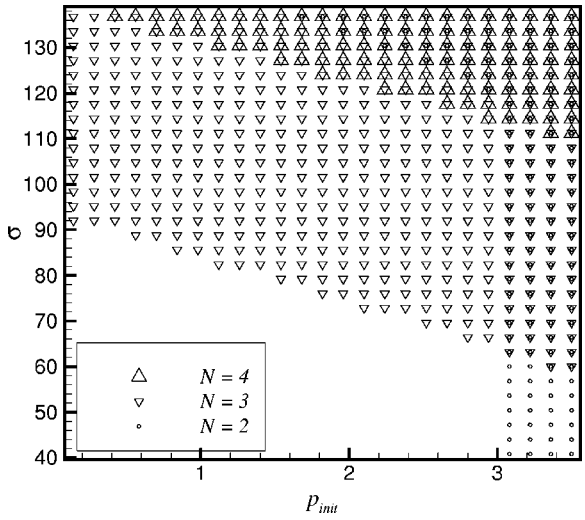

FIG. 8. The parameter values p_{init}, σ for which the system becomes unstable to nonaxisymmetric perturbations with azimuthal wavenumber N during the period $0<t^*/(\mu/K)<2.2\times10^4$. $H_0=0.1$, $L=\sqrt{2}\pi(1-H_0)$.

data shown in Fig. 7 to smaller and smaller values of σ. Furthermore, the nonaxisymmetric instability needs to develop over time scales that are comparable to the period T_{breath} of the breathing cycle if it is to be of relevance in the context of the airway closure problem. The estimates for physiological the parameter values discussed in Sec. V, show that the maximum nondimensional time of $t=t^*/(\mu/K)=2.2\times10^4$ in Fig. 7 corresponds to a dimensional value of 267 s which is much greater than T_{breath}. The value $\sigma_{min}\approx 63$ therefore presents a useful upper limit for the nondimensional surface tension below which airway closure cannot occur for the given values of H_0 and p_{init}. (A lower limit of $\sigma_{min}\approx 10$ can be derived by analyzing the static stability of the ultimate axisymmetric equilibrium state to nonaxisymmetric perturbations; see Appendix B).

A decrease in the initial pressure p_{init} has a similar effect to a decrease in σ. The onset of the nonaxisymmetric instability is delayed and its growth rate decreases. Again, there is a critical value of p_{init} below which the system does not become unstable to nonaxisymmetric perturbations. Figure 8 provides a summary of these results. A marker indicates a parameter combination (p_{init},σ) for which the system becomes unstable to nonaxisymmetric perturbations at some point during its axisymmetric evolution [the simulations were again carried out in the range $0<t^*/(\mu/K)<2.2\times10^4$]. For initial pressures in the range $p_{init}>3$, the tube is unstable to axially uniform buckling in the $N=2$ mode;[12] in these cases the axisymmetric redistribution of fluid is not required to initiate the nonaxisymmetric instability. For values of the initial pressure in the range $p_{init}<3$, the system first becomes unstable to buckling in the $N=3$ mode. The critical surface tension σ_{min} decreases with increasing p_{init}. At larger values of p_{init}, nonaxisymmetric perturbations with wavenumbers $N=2$ and $N=4$ also become unstable but, for a given combination of p_{init} and σ, the $N=3$ mode is always the first to become unstable; see Fig. 13 below.

A decrease in the initial film thickness H_0 (at constant p_{init}) decreases the growth rate of the primary axisymmetric

instability [see Eq. (22)], causing slower growths of the main lobe and the compression of the tube wall. Hence a decrease in H_0 delays the onset of the nonaxisymmetric instability and reduces its growth rate; for an illustration see Fig. 14 below.

Finally, we discuss the effect of variations in the domain length L. Thus far we have always assumed that the axial wavelength $\Lambda(=2L)$ of the nonaxisymmetric instability is identical to that of the fastest growing axisymmetric mode. If we shorten the computational domain, the axisymmetric instability develops with the (smaller) growth rate of the fastest growing axisymmetric mode that "fits" into this domain, as predicted by (22). Therefore, the onset of the nonaxisymmetric instability is delayed and its growth rate decreases; ultimately, when $\Lambda < 2\pi(1+V_0-\tilde{H}_0)$ even the axisymmetric instability is suppressed. In that case, nonaxisymmetric instabilities only occur for $p_{init} > 3$. For axial wavelengths in the range $\Lambda > \Lambda_{max}$, the axisymmetric instability initially grows at a rate less than ω_{max}, causing the wall compression to increase more slowly. However, in the large-displacement regime, the main lobe can recruit more fluid from the satellite lobe. This allows the main lobe to grow more quickly. Overall, the nonaxisymmetric instability occurs slightly earlier and its growth rate increases slightly with Λ. An example of this is shown in Fig. 15 below.

B. Numerical simulation in the nonlinear regime

The linear stability analysis presented in the preceding section showed that the wall compression induced by the primary axisymmetric instability can initiate the nonaxisymmetric buckling of the airway wall. We will now follow the growth of this secondary instability into the nonlinear, large-displacement regime to determine whether the initial (small-amplitude) buckling of the airway wall can result in airway closure.

1. Discretization

The coupled discretization of the two-dimensional shell and lubrication theory equations (1) and (12) was performed by the same method that we employed in Sec. III B for the axisymmetric equations. The one-dimensional Hermite elements were replaced by isoparametric quadrilateral Hermite elements[22,23] and the computational domain (covering half of one lobe, as indicated by the wire mesh in Fig. 1) was typically discretized with 10×10 elements. The code was validated by computing the large-displacement postbuckling deformation of a finite-length tube with clamped ends, loaded by a constant external pressure, and comparing the results against the predictions from existing, independent codes.[23,24] Furthermore, we compared the results from the fully coupled code against the predictions from the linear stability analysis (see below) and against preliminary results from a full Navier-Stokes simulation of the problem; see Fig. 16 in Appendix A.

2. Results

Figure 9 shows the evolution of the eight control radii $R_1,\ldots,R_4$ and $R_{h1},\ldots,R_{h4}$ for the same parameter values that we used in Fig. 5. One-sixth of the domain was discretized and a small pressure perturbation of the form $\epsilon_p \cos(3x^2)$ with $\epsilon_p = 10^{-4}$ was added to the load vector $\mathbf{f}$ to initiate the controlled development of the nonaxisymmetric instability. Figure 9 shows the initial development of the axisymmetric instability which manifests itself by a decrease in $R_{h1} \approx R_{h2}$ while $R_{h3} \approx R_{h4}$ increase; there are corresponding (but much smaller) changes in the wall control radii $R_1,\ldots,R_4$; see also the 3D plots of the wall and air-liquid interfaces shown in Fig. 10.

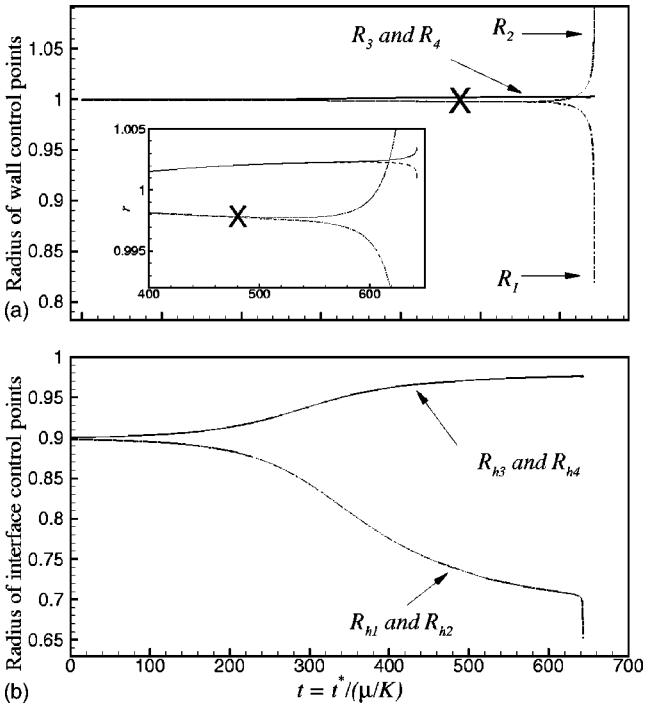

FIG. 9. (a) The tube wall control radii $R_1,\ldots,R_4$ and (b) fluid control radii $R_{h1},\ldots,R_{h4}$ against time. At $t\approx 480$, the tube begins to buckle nonaxisymmetrically in the $N=3$ mode. At $t\approx 640$, the system undergoes a rapid nonaxisymmetric collapse. Inset: The wall control radii $R_1,\ldots,R_4$ against time as the tube wall begins to buckle nonaxisymmetrically. The markers indicate the time at which the linear analysis predicts instability to nonaxisymmetric perturbations. $\sigma=100$, $p_{init}=2.9$, $H_0=0.1$, $L=\sqrt{2}\pi(1-H_0)$.

The inset in Fig. 9(a) shows a closeup of the evolution of the wall control radii in the vicinity of $t=480$—the time beyond which the (frozen-coefficient) linear stability analysis predicted positive growth rates for nonaxisymmetric perturbations with $N=3$ azimuthal waves (this time is also indicated by the marker). The inset indicates that the difference between the wall control radii R_1 and R_2 does indeed begin to grow exponentially at approximately this time. The nonaxisymmetric collapse remains localized and buckling only occurs in the vicinity of the main lobe—the cross section at $x=L$ remains approximately axisymmetric, $R_3 \approx R_4$; see also Fig. 10.

The contours in Fig. 11 illustrate the evolution of the normal component, $f_n = p_{ext} - \sigma\kappa_h$, of the load that acts on the wall. Initially, the wall is strongly compressed in the vicinity of the main lobe and inflated in the vicinity of the satellite lobe. As the wall begins to buckle nonaxisymmetrically, the pressure distribution in the region of the main lobe becomes highly nonuniform. The curvature of the air-liquid interface

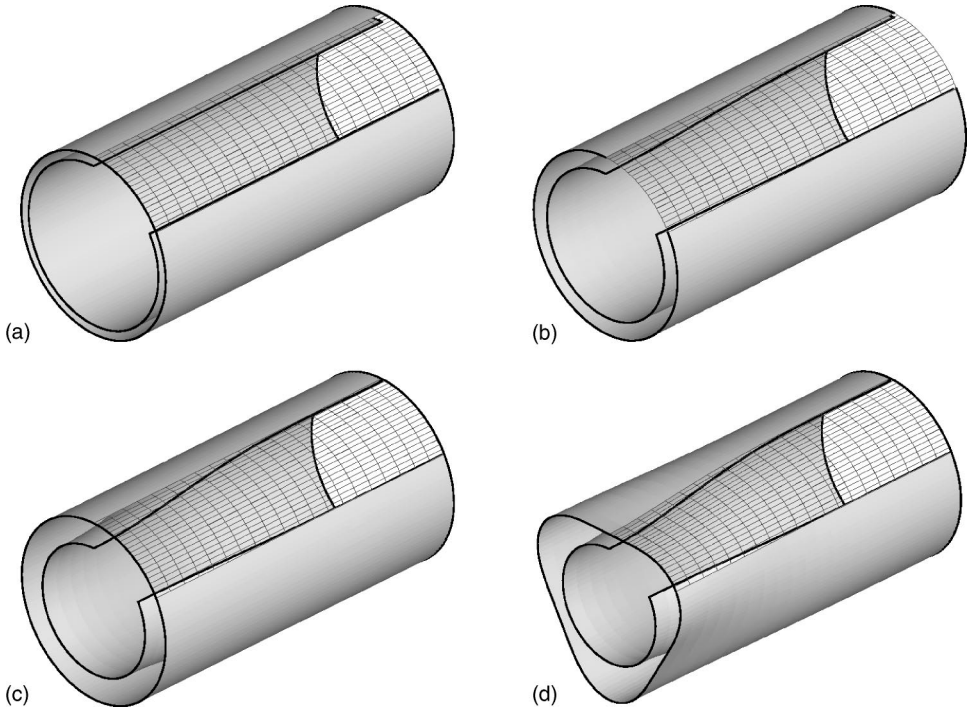

FIG. 10. The wall and air-liquid interface shapes at different times (a) $t=0$, (b) $t=345$, (c) $t=480$, and (d) $t=643$. The tube buckles nonaxisymmetrically in the $N=3$ mode. $H_0=0.1$, $\sigma=100$, $p_{init}=2.9$.

becomes more (less) negative in regions in which the wall buckles outwards (inwards). Since $p=\sigma\kappa_h$, this creates a fluid pressure gradient that drives azimuthal flows which attempt to return the air-liquid interface to an axisymmetric shape. Indeed, Fig. 10 shows that while the wall buckles strongly, the air-liquid interface remains nearly axisymmetric, $R_{h1}\approx R_{h2}$ and $R_{h3}\approx R_{h4}$. The azimuthal variations to the fluid pressure oppose the nonaxisymmetric wall deformations, as regions of the wall that buckle outwards are pulled inwards and vice versa. Compared to the case of a "dead" loading, the surface-tension-induced component of the load on the wall is therefore stabilizing and reduces the growth rate of the nonaxisymmetric instability. This effect was first reported in Ref. 12 for axially uniform instabilities.

As the nonaxisymmetric collapse increases, the small fluid pressure in the main lobe continues to drain fluid from the satellite lobe. Furthermore, the nonaxisymmetric buckling reduces the cross-sectional area of the most strongly collapsed cross section. These two effects continually reduce the radius of the air-liquid interface and cause a further increase in the compressive load on the wall in this region. Ultimately, this destabilizing feedback initiates a rapid nonaxisymmetric collapse of the tube and the air-liquid interface at $t\approx 640$. As in the axisymmetric case, the numerical simulation can only follow the compliant collapse up to a certain point. This is because the smaller and smaller time steps, required to resolve the extremely rapid collapse, ultimately cause numerical problems which result in the failure of the

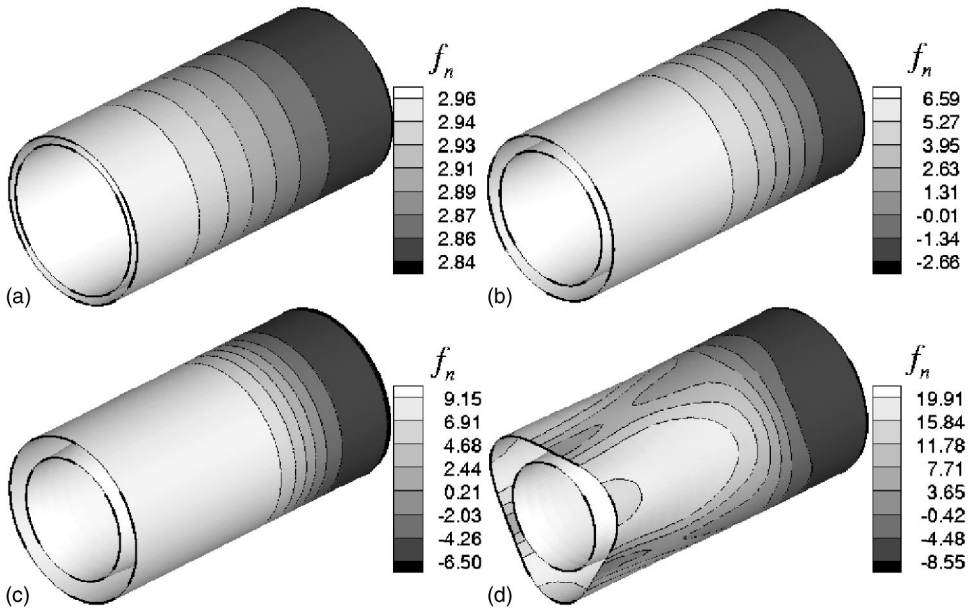

FIG. 11. Contour plots of the normal component of the load $f_n=p_{ext}-\sigma\kappa_h$ acting on the tube for (a) $t=0$, (b) $t=345$, (c) $t=480$, and (d) $t=643$. Note that the contour scales are different in each plot.

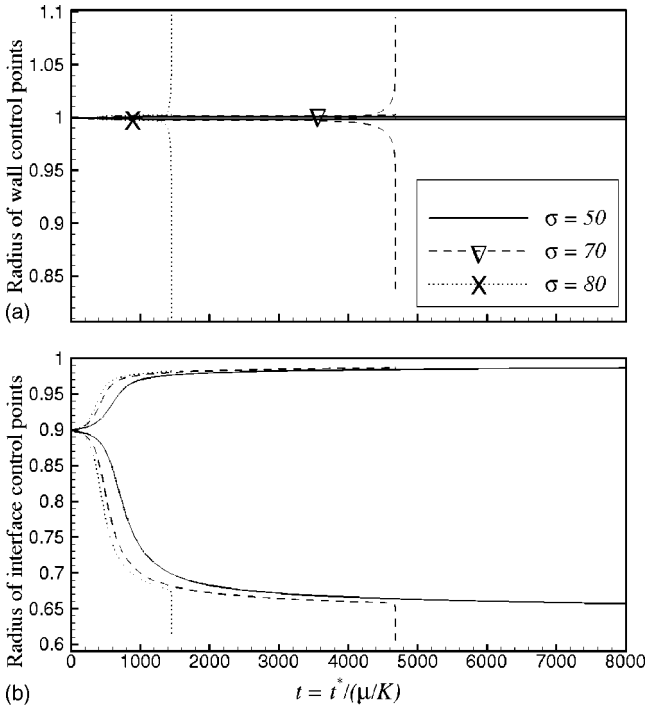

FIG. 12. (a) The wall control radii $R_1,\ldots,R_4$ and (b) the air-liquid interface control radii $R_{h1},\ldots,R_{h4}$ for different values of the nondimensional surface tension σ. The tube buckles in the $N=3$ mode in all cases. The markers indicate the time at which the linear analysis predicts instability to nonaxisymmetric perturbations. $H_0=0.1$, $p_{init}=2.9$, $L=\sqrt{2}\pi(1-H_0)$.

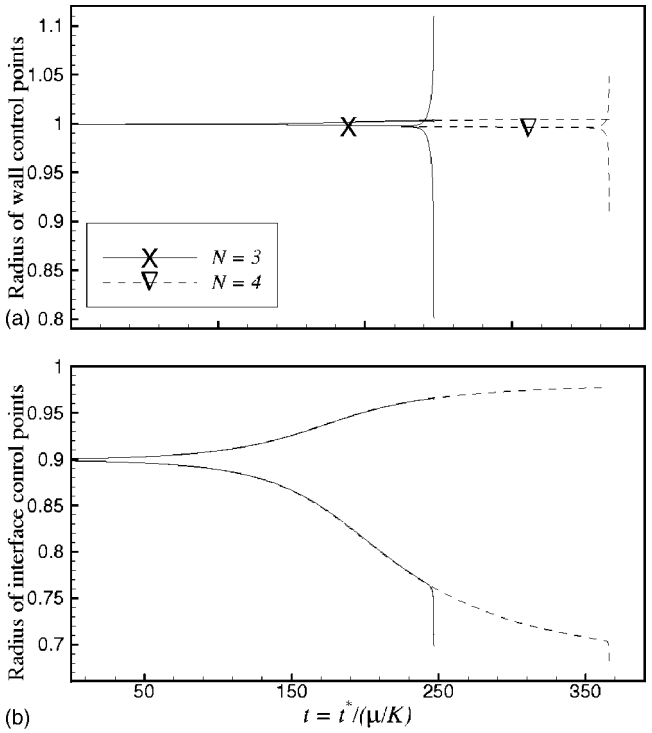

FIG. 13. (a) The wall radii $R_1,\ldots,R_4$ and (b) the air-liquid interface radii $R_{h1},\ldots,R_{h4}$ for instabilities with azimuthal wavenumbers $N=3$ and $N=4$. The markers indicate the time at which the linear analysis predicts instability to nonaxisymmetric perturbations. $\sigma=170$, $H_0=0.1$, $L=\sqrt{2}\pi(1-H_0)$.

Newton method to converge. However, full Navier–Stokes simulations of this problem for the same parameter values (see Fig. 16 in Appendix A) show that the system does indeed evolve towards a completely occluded state. This demonstrates that nonaxisymmetric instabilities allow the occurrence of airway closure in regions of parameter space in which axisymmetric models predict the airway to remain unoccluded (cf. Fig. 4).

Figure 12 illustrates the effect of variations in the nondimensional surface tension σ on the system's evolution in the large-displacement regime. For the parameter values chosen here, the linear stability analysis of Sec. IV A predicted an upper limit of $\sigma_{min}\approx 63$ for the minimum surface tension required for the nonaxisymmetric instability to occur. Figure 12 shows that the wall and the air-liquid interface do indeed remain axisymmetric for $\sigma=50$ [the simulation was continued until $t=t^*/(\mu/K)=5.0\times10^4$ and the small nonaxisymmetric perturbation induced by ϵ_p did not grow]. For $\sigma=70>\sigma_{min}$, the system becomes unstable to nonaxisymmetric perturbations at $t_{instab}\approx 3.6\times10^3$ and the final rapid collapse occurs at $t_{collapse}\approx 4.7\times10^3$. A further increase in σ reduces the time t_{instab} at which the system becomes unstable to small-amplitude nonaxisymmetric perturbations, as predicted by the results of the linear analysis in Fig. 7. Furthermore, the delay between the onset of the linear instability and the final catastrophic collapse decreases with an increase in σ. For instance, in Fig. 12, $t_{instab}-t_{collapse}\approx 1.1\times10^3$ for $\sigma=70$ and $t_{instab}-t_{collapse}\approx 3.5\times10^2$ for $\sigma=80$. This is caused by two effects: (i) For a given shape of the axisymmetric lobe, an increase in σ increases the additional wall compression; (ii) an increase in σ leads to a more rapid development of the primary axisymmetric instability; see Fig. 4. The combination of these effects implies that at larger σ, less time is required to reach the level of compression that is necessary to trigger first the nonaxisymmetric instability and then the ultimate catastrophic collapse. In all our simulations, the growth of small-amplitude, nonaxisymmetric perturbations ultimately led to nonaxisymmetric compliant collapse at a later time.

The linear stability analysis of Sec. IV A predicted that, at larger values of the surface tension, the system should become unstable to nonaxisymmetric perturbations in multiple modes (see, e.g., Fig. 8). An example of this is shown in Fig. 13 which illustrates the system's evolution in the large-displacement regime when the tube is subjected to perturbations with azimuthal wavenumbers $N=3$ and $N=4$, respectively (in the latter case, only one-eighth of the domain was discretized to accommodate perturbations with this wavenumber). The axisymmetric system is predicted to become unstable to perturbations with wavenumber $N=3$ at $t\approx 190$ and it undergoes a rapid nonaxisymmetric collapse at $t\approx 246$. For an $N=4$ perturbation, the linear instability is predicted to occur at the later time of $t\approx 321$ and the ultimate collapse only occurs at $t\approx 365$. We would therefore not expect to observe the $N=4$ instability in practice.

The effect of an increase in the initial film thickness H_0, illustrated in Fig. 14, is similar to that of an increase in σ. For larger values of H_0, the curvature of the air-liquid interface, and with it the wall compression, increases more rapidly. This causes the earlier onset of the nonaxisymmetric

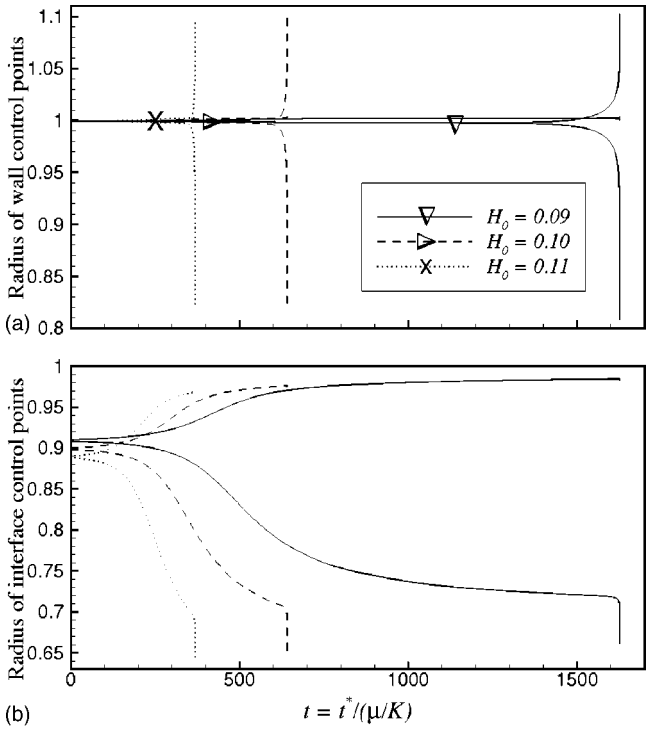

FIG. 14. Radius of control points for $H_0=0.09$, $H_0=0.1$, and $H_0=0.11$. The markers indicate the time at which the linear analysis predicts instability to nonaxisymmetric perturbations. In all cases $L=\sqrt{2}\pi(1-H_0)$, $\sigma=100$, $p_{init}=2.9$.

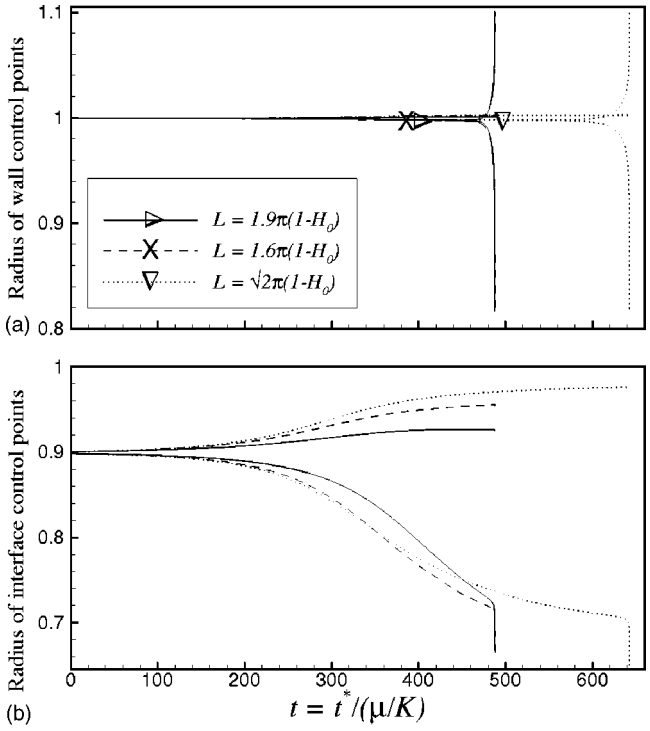

FIG. 15. (a) The wall control radii $R_1,\ldots,R_4$ and (b) the air-liquid interface control radii $R_{h1},\ldots,R_{h4}$ for different values of the tube length L. The tube buckles nonaxisymmetrically in the $N=3$ mode in all cases. $H_0=0.1$, $p_{init}=2.9$, $\sigma=100$.

instability (as predicted in Sec. IV A) and reduces the delay until the subsequent final collapse. Conversely, a reduction in H_0 delays the onset of the instability and the analysis presented in Appendix B shows that for a given value of the surface tension, there exists a critical film thickness below which the airway will remain open.

Figure 15 illustrates the effect of variations in the axial wavelength Λ of the nonaxisymmetric instability. As discussed in Sec. III, an increase in Λ beyond $\Lambda_{max}=2\sqrt{2}\pi(1-H_0)$ reduces the initial growth rate of the axisymmetric instability but leads to faster growth in the nonlinear regime. Figure 15 confirms that the perturbation with $L=\Lambda/2=1.9\pi(1-H_0)$ initially grows much more slowly than that with $L=\Lambda/2=1.6\pi(1-H_0)$, causing the instability to nonaxisymmetric perturbations to occur at $t\approx 420$, as opposed to $t\approx 400$. However, in the large-displacement regime, the perturbation with the larger wavelength grows much more quickly and for both wavelengths, the ultimate collapse occurs at approximately the same time $t\approx 488$, much earlier than for the initially fastest growing mode.

Finally, we discuss the effect of variations in the wall stiffness K. For given values of the dimensional surface tension σ^*, the film thickness H_0, and the external pressure p^*_{ext}, the primary effect of a reduction in K (corresponding to a weakening of the airway walls) is an increase in the nondimensional surface tension σ and the initial load p_{init}. This makes the airway more susceptible to buckling instabilities. When we analyzed the effect of variations in σ on the system's postbuckling behavior, we have (so far) always associated changes in σ with changes in the dimensional surface tension σ^*. An increase in the nondimensional surface tension σ via a reduction in wall stiffness has two competing effects. While the increase in σ leads a faster growth of the instabilities on the time-scale $T=\mu/K$ (see Figs. 2, 7, and 12), the time-scale T itself increases as well. Rescaling our results onto the bending-stiffness-independent time-scale $T_{visc}=\sigma T$ shows that an increase in σ via a reduction in K still leads to an overall increase in the growth rates of the primary and secondary instabilities.

V. SUMMARY AND DISCUSSION

Motivated by the problem of pulmonary airway closure, we have studied three-dimensional nonaxisymmetric instabilities of liquid-lined elastic tubes. The system's evolution is driven by gradients in its total potential energy (comprising the strain energy stored in the elastic wall and the surface energy stored in the air-liquid interface). Hence static analyses, such as those in Refs. 10, 11, 13, and 14 can identify the system's (possibly multiple) equilibrium configurations and their stability to quasisteady, small-amplitude perturbations. However, only dynamic analyses, such as the one performed here, can determine which of these equilibrium configurations can be realized via a continuous evolution from a given initial state. Furthermore, dynamic analyses are required to establish the time scales over which any instabilities develop. Appendix B shows that, in the present problem, a quasistatic stability analysis leads to unrealistically small values of the surface tension σ_{min} required for airway closure to occur.

We have shown that the additional wall compression induced by a primary, axisymmetric fluid-elastic instability can

initiate the nonaxisymmetric buckling of a liquid-lined airway and that the nonlinear growth of this secondary instability can initiate a compliant collapse. Our simulations demonstrate that the nonaxisymmetric instability mechanism allows the occurrence of airway closure at fluid volumes that are too small to occlude an airway in its axisymmetric state. Furthermore, even in cases in which the surface tension and the initial film thickness are large enough to allow the occurrence of airway closure by the axisymmetric instability mechanism, nonaxisymmetric instabilities will cause airway closure at much earlier times. For instance, for $H_0=0.1$, $\sigma=520$, Fig. 4, predicts axisymmetric airway closure to occur at $t^*/(\mu/K)\approx 1.14\times 10^3$. The analysis of Sec. IV A predicts that the evolving system will become linearly unstable to nonaxisymmetric perturbations at $t_{instab}\approx 37.5$ and the numerical simulation of the nonlinear evolution shows that nonaxisymmetric airway closure occurs at $t_{collapse}\approx 58.7$, long before an axisymmetric occlusion forms.

To assess the significance of our results in the physiological context, we use Halpern and Grotberg's[7] estimates for the parameter values in the terminal bronchioli, namely, $R_0=250$ μm, $\sigma^*=20$ dynes/cm, $\mu=10^{-3}$ kg/(m s), $E=6\times 10^4$ dynes/cm^2, $\nu=0.49$, and $h/R_0=1/10$. This corresponds to a nondimensional surface tension of $\sigma=120$ and time scale of $T=\mu/K=1.5\times 10^{-3}$ s. Hence the simulations presented in the previous sections were performed with physiologically relevant parameter values. Moreover, airway closure by the 3D instability mechanism occurs over time scales that are shorter than (or comparable to) the period of the breathing cycle. For instance, for the parameter estimates listed above, the dimensional time from the start of the simulation to the ultimate collapse is $t=t^*/(\mu/K)\approx 310$ which corresponds to a dimensional closure time of ≈ 0.47 s.

Our results are consistent with clinical observations since they show the susceptibility to airway closure to be enhanced by an increase in surface tension (e.g., in respiratory distress syndrome), by an increase in the initial thickness of the liquid lining (e.g., in pulmonary edema), and by a structural weakening of the airway walls. All three effects cause an increase in the initial compression of the airway and thus render the wall more liable to buckling instabilities. Additionally, these effects lead to a much faster growth of the nonaxisymmetric instabilities when they develop.

The film thicknesses used in the simulations presented here are larger than those typically encountered in the axially uniform liquid lining of a healthy lung (see, e.g., Ref. 25). We expect the results presented in this study to be mainly applicable to situations in which diseases such as edema have led a noticeable thickening of the liquid lining. This is because, even though the nonaxisymmetric instabilities also develop at much smaller film thicknesses, the time scale for their growth becomes much larger than the period of the breathing cycle. The development of the instability is therefore likely to be affected by the periodic expansion and contraction of the airways, an effect that we have neglected in our model.

In an attempt to keep our theoretical model as simple as possible, we have only incorporated those physical effects that we believe to be of primary importance for the development of the nonaxisymmetric instabilities. We have ignored the presence of surfactants and have assumed that the surface tension σ^* remains constant. Reduced surfactant production in the lung is known to cause severe respiratory problems (e.g., in neonatal respiratory distress syndrome) and within the framework of our model this can be attributed to the global increase in surface tension which was shown to facilitate the occurrence of airway closure. The presence of surfactant also affects the dynamics of surface-tension-driven flows and this effect has not been included in our model. Halpern and Grotberg[26] showed that, in their axisymmetric model, the presence of surfactant reduces the growth rate of the primary axisymmetric instability, which would delay the onset of the secondary instability and therefore be likely to increase the time to closure.

Our model ignored the effect of van der Waals forces which may be important in regions in which the film thickness becomes very small. As discussed in Sec. III, film rupture during the evolution of the primary axisymmetric instability would stop the draining flows from the satellite to the main lobe. This would lead to an axisymmetric equilibrium state with multiple static lobes, separated by "dry" regions. The volume of fluid contained in the lobes would depend on the precise moment at which film rupture occurred. It is more difficult to anticipate the effect of film rupture during the evolution of the nonaxisymmetric instability. Initially, the film would only rupture at isolated points and rupture would not necessarily cause the breakup of the film into multiple disconnected regions. While the incorporation of van der Waals forces into our model would be relatively straightforward, it is not clear if this would genuinely improve the description of the physics involved in the airway closure problem. We believe that the detailed topology of the airway wall (which does not have a smooth surface as assumed here) would begin to affect the fluid flow long before van der Waals forces become important.

Our model of the airway wall neglected its multilayer internal structure,[27] its viscoelastic behavior, and the effects of external tethering. These effects will influence the parameter values for which airway closure can occur and the time scale over which it develops. Nevertheless, we believe that none of these effects will be able to completely suppress the airway closure mechanism analyzed here. Once the radius of the air-liquid interface has been reduced sufficiently (possibly by applying a relatively larger external pressure to overcome the additional stiffness provided by the external tethering), the rapid increase in the pressure jump over the highly curved air-liquid interface cannot possibly be balanced by any of these restoring (or retarding) forces.

The external tethering and the multilayer structure of the airway wall could, however, lead to a change in the most unstable azimuthal wavenumber N. References 27 and 28 demonstrated (in two-dimensional geometries) that both effects tend to cause an increase in N, and physiological observations[29] do indeed suggest that airways buckle with larger wavenumbers than predicted by our model.

Finally, we note that our analysis was performed with periodic boundary conditions whereas the bronchial airways branch frequently. Our simulations predict airway closure to

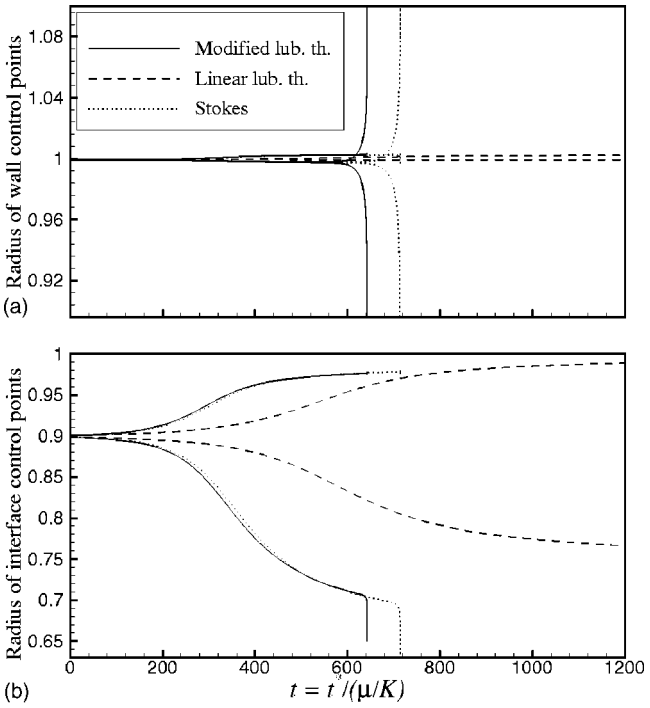

FIG. 16. Comparison of lubrication theory, using the full nonlinear expressions for M and κ_h, Stokes flow, and classical lubrication theory with linearized expressions for κ_h and M. $H_0=0.1$, $p_{init}=2.9$, $\sigma=100$.

occur in a highly localized fashion (typically, the buckling region extends over two to three airway diameters). Hence, if the occlusion develops in the central part of an individual airway, the support provided by the bifurcations is unlikely to have a major effect on the instability discussed here.

ACKNOWLEDGMENTS

Financial support from the EPSRC for a Project Studentship for J.P.W. and an Advanced Fellowship for M.H. is gratefully acknowledged. The authors also wish to thank Dr. Andrew Hazel for many helpful discussions. The HSL library routine HSL_MA42 (a frontal solver for sparse, unsymmetric systems[19]) was used in this work.

APPENDIX A: VALIDATION AND COMPARISON WITH 3D STOKES FLOW SIMULATIONS

Figure 16 shows the evolution of the control radii for the same parameter values that were used in Fig. 9. The solid lines represent the results obtained from the lubrication theory model (12) while the dotted lines were obtained from a full 3D Stokes flow simulation (performed by Hazel and Heil; see Ref. 20 for further details of the comparison). Even though the initial film thickness $H_0=0.1$ is rather large (by the standards of "classical" lubrication theory), the use of the exact nonlinear expressions for M and κ_h in Eq. (12) ensures that the agreement with the full Stokes flow simulation is very good. The two simulations only differ significantly in their predictions of the time $t_{collapse}$ at which the final catastrophic collapse occurs. While the occurrence (or nonoccurrence) of the nonaxisymmetric compliant collapse can be predicted with either code, the precise value of $t_{collapse}$ is very sensitive to slight changes in the load on the wall. The slight differences between the fluid tractions predicted by the lubrication theory model and the full Stokes equations during $t < t_{collapse}$ are therefore sufficient to delay the occurrence of the final collapse in the Stokes flow simulation by a finite amount.

Figure 16 also shows the predictions obtained from the classical lubrication theory model in which the expressions for κ_h and M in (12) were linearized with respect to the wall displacements and the film thickness. This model already provides a poor description of the system's axisymmetric evolution and completely fails to capture the nonaxisymmetric instability and the ultimate collapse.

APPENDIX B: A LOWER BOUND FOR σ_{min}

In Sec. IV A we defined σ_{min} as the value of the nondimensional surface tension, below which the airway never becomes unstable to nonaxisymmetric perturbations. We determined an upper limit of $\sigma_{min}\approx 63$ (for $H_0=0.1$ and $p_{init}=2.9$) by monitoring the stability of the evolving axisymmetric configuration up to a time of $t=t^*/(\mu/K)=2.2\times 10^4$. Even after such large times, the system continues to evolve and the curvature of the air-liquid interface continues to increase, albeit very slowly, in the region of the main lobe. Therefore, at even larger times, nonaxisymmetric instabilities may still occur at smaller values of σ.

We will now derive a lower limit for σ_{min} by investigating the (static) stability of the system's final axisymmetric equilibrium configurations to nonaxisymmetric perturbations. As $t\to\infty$, the satellite lobe completely drains into the main lobe whose air-liquid interface adopts a shape of constant curvature, κ_{und}. The main lobe only wets the wall over a finite length $\Lambda_{und}<\Lambda$. We assume that the air-liquid interface joins the dry wall at zero contact angle and neglect the effect of the small axisymmetric wall deformations on the air-liquid interface shape. Figure 17 illustrates the possible axisymmetric equilibrium configurations that a liquid film of initial thickness H_0 can evolve towards when it is subjected to an initial perturbation with axial wavelength Λ.

Figure 18 shows the interface curvature κ_{und} and the axial length Λ_{und} of these equilibrium configurations as a function of the wavelength Λ, for a film of initial thickness $H_0=0.1$. Curve I represents the uniform liquid film [of constant curvature $\kappa_{und}=-1/(1-H_0)$ and length $\Lambda_{und}=\Lambda$]. This configuration becomes unstable beyond point A, when $\Lambda > 2\pi(1-H_0)$. Curve II shows the curvature and length of an unduloid-shaped air-liquid interface that encloses the same volume of fluid as the uniform liquid film (see Ref. 2). For a range of wavelengths, two different unduloids exist. At the lower end of this curve (point C), the unduloid degenerates into a minimal occluding liquid bridge (of curvature $\kappa_{und}=-2$ and length $\Lambda_{und}=2$; state III in Fig. 17). For $\Lambda > 2/3H_0(2-H_0)$, curve III in Fig. 18 represents occluding liquid bridges of finite thickness.

Everett and Haynes[2] determined the stability of these equilibria to constant-volume perturbations by considering the "effective area" of the various configurations. In Fig. 18 markers indicate configurations that are stable to small am-

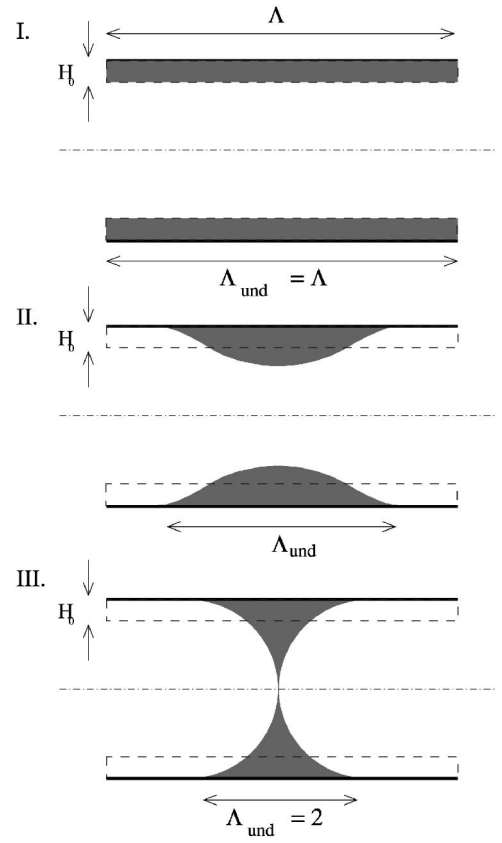

FIG. 17. Sketch of the possible axisymmetric equilibrium configurations. (I) A uniform liquid film; (II) a finite-length unduloid; (III) an occluding liquid bridge; shown here as a minimal liquid bridge.

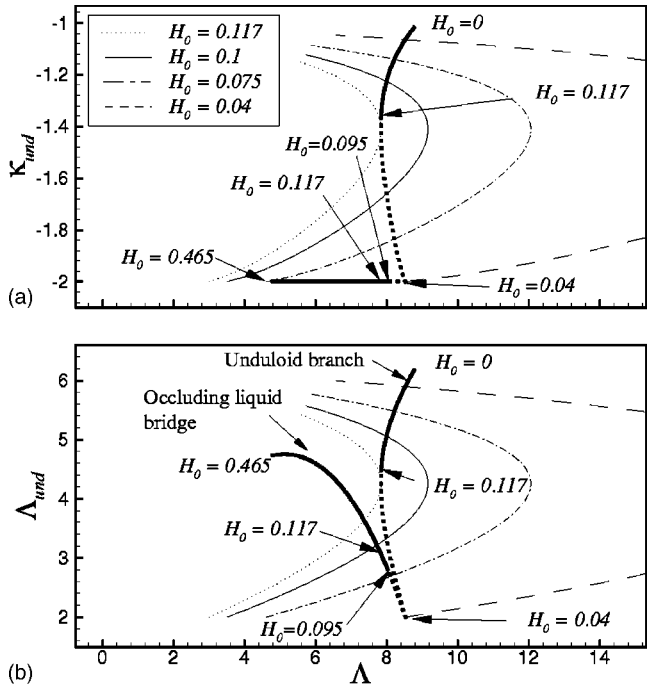

FIG. 19. The thin lines show (a) the curvature κ_{und} and (b) the length Λ_{und} of the unduloid that develops when a uniform liquid film of initial thickness H_0 undergoes an axisymmetric instability of wavelength Λ. The thick line **E** indicates parameter combinations for which $\Lambda=2\sqrt{2}\pi(1-H_0)$ and thus corresponds to configurations that develop from the fastest growing perturbation to the initially uniform liquid film. The solid and dotted parts of this curve indicate stable and unstable configurations.

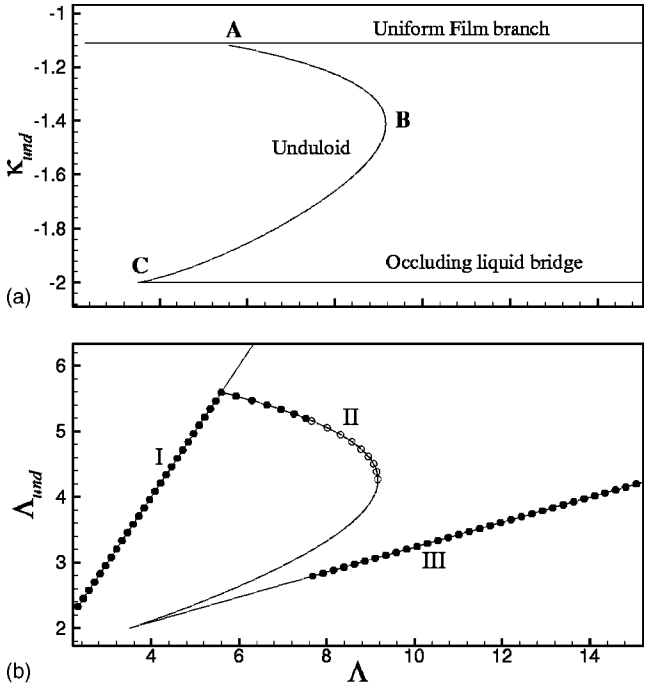

FIG. 18. (a) Curvature κ_{und} and (b) length Λ_{und} of the equilibrium configurations that have the same volume of fluid as a uniform liquid film of initial thickness $H_0=0.1$ and (wave)length Λ. The markers in (b) indicate stable equilibria; hollow markers indicate metastable states.

plitude perturbations. In a certain range of wavelengths ($7.65<\Lambda<9.17$), identified by the hollow markers, the occluding liquid bridge configuration has a smaller effective area than the corresponding (metastable) unduloid but finite amplitude perturbations are required to allow a continuous transition between these two states. For $\Lambda>9.17$, the unduloid no longer exists and the only nontrivial equilibrium state is the occluding liquid bridge.

The thin lines in Fig. 19 show the same curves as in Fig. 18 for a number of different initial film thicknesses H_0 (for clarity only the unduloid branch II is shown). The thick line, **E**, indicates parameter combinations for which $\Lambda=2\sqrt{2}\pi(1-H_0)$ and thus identifies the possible final equilibrium configurations for axisymmetric instabilities that originate from the fastest growing perturbation to the initial, uniform state. The dotted parts of the curve represent unstable equilibria.

For thin films, $0<H_0<0.117$, the fastest growing perturbation to the uniform film will evolve towards an unduloid. The occluding liquid bridge represents a possible equilibrium state for $H_0>0.04$, but it is stable only for $H_0>0.095$. Furthermore, it can only be realized in a continuous evolution from the axially uniform state for $H_0>0.117$. Films of greater thickness evolve towards stable occluding liquid bridges of increasing thickness.

When the axisymmetric instability has evolved towards its final, stable equilibrium state, the load on the axisymmetric wall is therefore given by

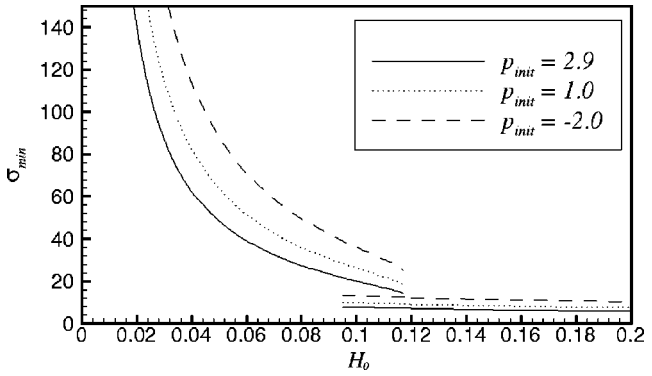

FIG. 20. The lower limit for σ_{min} as a function of the initial film thickness H_0 for various values of p_{init}. $\Lambda = 2\sqrt{2}\pi(1-H_0)$.

$$\mathbf{f} = \begin{cases} -(p_{ext} - \sigma\kappa_{und})\mathbf{N} & \text{if } 0 \leqslant |x^1| \leqslant \Lambda_{und}, \\ -p_{ext}\mathbf{N} & \text{if } \Lambda_{und} < |x^1| \leqslant \Lambda, \end{cases} \tag{B1}$$

where, for a given value of H_0, the values of Λ_{und} and κ_{und} are given by the solid part of the line **E** in Fig. 19.

We insert this (static) load into (1) and investigate the stability of the wall's axisymmetric state by the procedure described in Sec. IV A. In the present case, the governing equations have no time dependence, therefore the finite element discretization of the $O(\epsilon)$ equations yields a standard eigenvalue problem of the form $\mathbf{Ax}=\mathbf{0}$. The condition for instability, $\det(\mathbf{A})=0$, establishes the values of σ for which the axisymmetric equilibrium state becomes unstable to nonaxisymmetric perturbations of a given azimuthal wavenumber N. We regard the smallest value of σ as a lower limit for σ_{min}.

Figure 20 illustrates the dependence of σ_{min} on the value of the initial thickness H_0 and the initial pressure p_{init}. In all cases, $N=3$ represented the most unstable azimuthal wavenumber. For small values of H_0 the axisymmetric perturbation evolves towards an unduloid of small negative curvature. Hence, relatively large surface tensions are required to cause nonaxisymmetric buckling. As the film thickness is increased, κ_{und} becomes more negative (see Fig. 19), causing σ_{min} to decrease.

The stable occluding liquid bridge configurations that exist once $H_0 > 0.095$ have a large negative curvature of $\kappa_{und}=-2$. In this configuration, only very small surface tensions of $\sigma_{min} \approx 10$ are required to cause the buckling of the airway wall. These values of σ_{min} are consistent with those obtained in Ref. 11 where only buckling in the $N=2$ mode was considered. An increase in H_0 increases the length, Λ_{und}, over which the occluding liquid bridges wet the wall and expose it to their compressive load; see Fig. 19(b). This leads to a slight reduction in σ_{min} with a further increase in H_0. An increase in p_{init} decreases the value of σ_{min} because the load on the tube depends linearly on the external pressure.

Finally, we note that, for a given value of the surface tension σ, the lines in Fig. 20 can also be interpreted as predictions of the minimum film thickness H_0 required for nonaxisymmetric airway closure to be possible.

APPENDIX C: COMPARISON WITH HALPERN AND GROTBERG

In this appendix, we provide a more detailed comparison between the results presented in Sec. III and those obtained previously by Halpern and Grotberg (HG) in their study of axisymmetric airway closure.[7] HG's wall model incorporated the effects of axial prestress, wall damping, and azimuthal (hoop) stress. In an attempt to keep our model as simple as possible, the first two of these effects were ignored in our study. HG's wall-stiffness parameter Γ can be related to the nondimensional surface tension σ via $\Gamma \approx 1/12(h_w/R_0)^2\sigma$. The values of σ used in our study are at the low (and physiologically appropriate) end of the range explored in HG's study and in this regime HG's analysis agrees with the results presented in Sec. III: wall elasticity leads to a small increase in the growth rates of the axisymmetric instability (see, e.g., HG's Fig. 6 for $\Gamma=0.1$ which corresponds to $\sigma \approx 120$). The infinite growth rates that HG predicted for certain finite-wavelength perturbation at zero wall damping, only occur at large (and, in the context of the physiological problem, probably somewhat unrealistic) values of Γ.

Direct comparisons between the finite-amplitude simulations are difficult because HG only provide detailed illustrations of the nonlinear evolution for cases with large wall damping. While this precludes direct comparisons, Fig. 9 in their paper shows that the rapid ultimate snap-off towards an axisymmetric occlusion occurs if and when the Rayleigh instability reduces the minimum radius of the air-liquid interface to $R_{min} \approx 0.5$. This is consistent with the results shown in Fig. 4 in the present paper.

[1] J. B. Grotberg, "Pulmonary flow and transport phenomena," Annu. Rev. Fluid Mech. **26**, 529 (1994).
[2] D. H. Everett and J. M. Haynes, "Model studies of capillary condensation. I. Cylindrical pore model with zero contact angle," J. Colloid Interface Sci. **28**, 125 (1972).
[3] S. L. Goren, "The instability of an annular thread of fluid," J. Fluid Mech. **12**, 309 (1962).
[4] P. S. Hammond, "Non-linear adjustment of a thin annular film of viscous fluid surrounding a thread of another within a circular cylindrical pipe," J. Fluid Mech. **137**, 363 (1983).
[5] M. Johnson, R. D. Kamm, L. W. Ho, A. Shapiro, and T. J. Pedley, "The nonlinear growth of surface-tension-driven instabilities of a thin annular film," J. Fluid Mech. **233**, 141 (1991).
[6] J. M. B. Hughes, D. Y. Rosenzweig, and P. B. Kivitz, "Site of airway closure in excised dog lungs: histologic demonstration," J. Appl. Physiol. **29**, 340 (1970).
[7] D. Halpern and J. B. Grotberg, "Fluid-elastic instabilities of liquid-lined flexible tubes," J. Fluid Mech. **244**, 615 (1992).
[8] R. D. Kamm and R. C. Schroter, "Is airway closure caused by a liquid film instability?" Respir. Physiol. **75**, 141 (1989).
[9] P. A. Gauglitz and C. J. Radke, "An extended evolution equation for liquid film breakup in cylindrical capillaries," Chem. Eng. Sci. **43**, 1457 (1988).
[10] M. Heil, "Airway closure: Liquid bridges in strongly buckled elastic tubes," ASME J. Biomech. Eng. **121**, 487 (1999).
[11] M. Heil, "Minimal liquid bridges in non-axisymmetrically buckled elastic tubes," J. Fluid Mech. **380**, 309 (1999).
[12] M. Heil and J. P. White, "Airway closure: Surface-tension-driven nonaxisymmetric instabilities of liquid-lined elastic rings," J. Fluid Mech. **462**, 79 (2002).
[13] M. J. Hill, T. A. Wilson, and R. K. Lambert, "Effect of surface tension and intraluminal fluid on mechanics of small airways," J. Appl. Physiol. **82**, 233 (1997).
[14] J. Rosenzweig and O. E. Jensen, "Capillary-elastic instabilities of liquid-lined airways," ASME J. Biomech. Eng. **124**, 650 (2002).
[15] G. A. Wempner, *Mechanics of Solids with Applications to Thin Bodies*.

(Sijthoff and Noordhoff, Alphen aan den Rijn, 1981).
[16] J. L. Sanders, "Nonlinear theories for thin shells," Q. J. Mech. Appl. Math. **21**, 21 (1963).
[17] S. Middleman, *Modeling Axisymmetric Flows: Dynamics of Films, Jets, and Drops* (Academic, San Diego, 1995).
[18] P. Gresho and R. Sani, *Incompressible Flow and the Finite Element Method* (Wiley, Chichester, 2000).
[19] ANONYMOUS 2000 A collection of Fortran codes for large scale scientific computation; http://www.numerical.rl.ac.uk
[20] J. P. White, "Airway closure: Surface-tension-driven non-axisymmetric instabilities of liquid-lined elastic tubes," Ph.D. thesis, University of Manchester, Manchester, 2003.
[21] T. A. I. Akeju, "Approximations of the buckling stresses of cylinders to unform external normal pressure," ASME J. Appl. Mech. **43**, 517 (1976).
[22] F. K. Bogner, R. L. Fox, and L. A. Schmit, "A cylindrical shell discrete element," AIAA J. **5**, 645 (1967).
[23] M. Heil and T. J. Pedley, "Large postbuckling deformations of cylindrical shells conveying viscous flow," J. Fluids Struct. **10**, 565 (1996).
[24] A. L. Hazel and M. Heil, "Three-dimensional airway reopening: The steady propagation of a semi-infinite bubble into a buckled elastic tube," J. Fluid Mech. **478**, 47 (2003).
[25] J. Bastacky, C. Y. C. Lee, J. Goerke, H. Koushafar, D. Yager, I. Kenaga, T. P. Speed, Y. Chen, and J. A. Clements, "Alveolar lining layer is thin and continuous—low-temperature scanning electron-microscopy of rat lung," J. Appl. Physiol. **79**, 1651 (1995).
[26] D. Halpern and J. B. Grotberg, "Surfactant effects on fluid-elastic instabilities of liquid-lined elastic tubes: a model for airway closure," ASME J. Biomech. Eng. **115**, 271 (1993).
[27] B. R. Wiggs, C. A. Hrousis, J. M. Drazen, and R. D. Kamm, "On the mechanism of mucosal folding in normal and asthmatic airways," J. Appl. Physiol. **83**, 1814 (1997).
[28] C. Y. Wang, L. T. Watson, and M. P. Kamat, "Buckling, postbuckling, and the flow through a tethered elastic cylinder under external pressure," ASME J. Appl. Mech. **50**, 13 (1983).
[29] R. K. Lambert, S. L. Codd, M. R. Alley, and R. J. Pack, "Physical determinants of bronchial mucosal folding," J. Appl. Physiol. **77**, 1206 (1994).